

Intrinsic higher-order topological states in two-dimensional honeycomb quantum spin Hall insulators

Sibin Lü(吕思彬) and Jun Hu(胡军)

Citation: Chin. Phys. B, 2025, 34 (**11**): 117303. DOI: 10.1088/1674-1056/addcd2
http://cpb.iphy.ac.cn; http://iopscience.iop.org/cpb

What follows is a list of articles you may be interested in

Doping-induced magnetic and topological transitions in $Mn_2X_2Te_5$ (X = Bi, Sb) bilayers

Wei Chen(陈威), Chuhan Tang(唐楚涵), Chao-Fei Liu(刘超飞), and Mingxing Chen(陈明星)
Chin. Phys. B, 2025, 34 (**9**): 097304. DOI: 10.1088/1674-1056/ade4af

Random flux manipulating topological phase transitions in Chern insulators

Jinkun Wang(王锦坤) and Wu-Ming Liu(刘伍明)
Chin. Phys. B, 2025, 34 (**6**): 067301. DOI: 10.1088/1674-1056/adc36a

Higher-order topological corner states and origin in monolayer LaBrO

Qing Wang(王庆) and Ning Hao(郝宁)
Chin. Phys. B, 2024, 33 (**12**): 127303. DOI: 10.1088/1674-1056/ad8a50

Quantum spin Hall insulators in chemically functionalized As (110) and Sb (110) films

Xiahong Wang(王夏烘), Ping Li(李平), Zhao Ran(冉召), Weidong Luo(罗卫东)
Chin. Phys. B, 2018, 27 (**8**): 087305. DOI: 10.1088/1674-1056/27/8/087305

Two-dimensional topological insulators with large bulk energy gap

Z Q Yang(杨中强), Jin-Feng Jia(贾金锋), Dong Qian(钱冬)
Chin. Phys. B, 2016, 25 (**11**): 117312. DOI: 10.1088/1674-1056/25/11/117312

Intrinsic higher-order topological states in two-dimensional honeycomb quantum spin Hall insulators

Sibin Lü(吕思彬) and Jun Hu(胡军)†

Institute of High Pressure Physics, School of Physical Science and Technology, Ningbo University, Ningbo 315211, *China*

(Received 5 April 2025; revised manuscript received 23 May 2025; accepted manuscript online 26 May 2025)

The exploration of topological phases remains a cutting-edge research frontier, driven by their promising potential for next-generation electronic and quantum technologies. In this work, we employ first-principles calculations and tight-binding modeling to systematically investigate the topological properties of freestanding two-dimensional (2D) honeycomb Bi, HgTe, and Al_2O_3(0001)-supported HgTe. Remarkably, all three systems exhibit coexistence of intrinsic first- and higher-order topological insulator states, induced by spin–orbit coupling (SOC). These states manifest as topologically protected gapless edge states in one-dimensional (1D) nanoribbons and symmetry-related corner states in zero-dimensional (0D) nanoflakes. Furthermore, fractional electron charges may accumulate at the corners of armchair-edged nanoflakes. Among these materials, HgTe/Al_2O_3(0001) is particularly promising due to its experimentally feasible atomic configuration and low-energy corner states. Our findings highlight the importance of exploring higher-order topological phases in quantum spin Hall insulators and pave the way for new possibilities in device applications.

Keywords: higher-order topological insulators, two-dimensional honeycomb lattice, quantum spin Hall insulators

PACS: 73.20.At, 73.22.–f, 03.65.Vf

DOI: 10.1088/1674-1056/addcd2 **CSTR:** 32038.14.CPB.addcd2

1. Introduction

Topological insulators (TIs), characterized by the quantum spin Hall (QSH) effect, have received extraordinary attention over the past decade due to their unique electronic properties, which hold great promise for the development of next-generation electronic and spintronic devices, as well as quantum computing.[1–4] Typically, a d-dimensional TI manifests SOC induced gapless and dissipationless boundary states in its $(d-1)$-dimensional counterparts, giving rise to a nonzero integer topological invariant $\mathbb{Z}_2$. To date, numerous TIs have been reported in both 2D and three-dimensional (3D) forms.[5–7] These TIs are now classified as $\mathbb{Z}_2$ TIs or first-order TIs (FOTIs), a categorization refined by the recent theoretical proposal of higher-order TIs (HOTIs).[8–11] Specifically, two-dimensional $\mathbb{Z}_2$ TIs are also known as QSH insulators. In general, a d-dimensional n-th-order TI hosts topologically protected gapless boundary states in its $(d-n)$-dimensional form, while remaining gapped in other dimensions. For instance, 2D HOTIs display topological corner state, whereas their one-dimensional (1D) counterparts, such as nanoribbons and nanowires, are lack of nontrivial gapless edge states, thereby distinguishing them from conventional 2D $\mathbb{Z}_2$ TIs.

Despite extensive theoretical proposals[8–17] and experimentally realizations in artificially synthesized acoustic and photonic systems,[18] the discovery of realistic crystalline materials that host HOTI states remains limited. Graphene, the first predicted 2D $\mathbb{Z}_2$ TI, was later predicted to be an HOTI, with topological corner states appearing in diverse geometric configurations such as triangles, rhombuses, and hexagons.[19] Similarly, other carbon allotropes, including γ-graphyne and graphdiyne, that were regarded as normal insulators due to their zero topological invariant number (i.e., $\mathbb{Z}_2 = 0$), have also been predicted to be HOTIs.[20–24] Additionally, twisted bilayer graphene at specific twisting angles has been suggested to host topological corner states.[25,26] Other systems such as the Sierpiński lattice and superconductor/topological-insulator/superconductor junctions were revealed to exhibit topological corner states.[27,28] Furthermore, certain 3D materials, such as bulk Bi and the magnetic axion insulator $Bi_{2-x}Sm_xSe_3$, have been identified as HOTIs, exhibiting hinge states in their 1D counterparts.[29,30] Fractal nanostructures in Bi thin films have also been observed to support robust corner states.[31] Obviously, these findings underscore the importance of further exploration of HOTIs for both fundamental research and potential applications.

Given the abundance of conventional $\mathbb{Z}_2$ TIs, a natural question arises: can HOTI states intrinsically emerge within them? In fact, bismuthene, an intrinsic QSH insulator, has been predicted to host topological corner states when time-reversal symmetry is broken via magnetic substrates or in-plane magnetic fields.[32,33] In addition, in bilayer systems formed by stacking two QSH insulators, interlayer coupling can induce topological corner states.[34] In these cases, FOTI states are intentionally suppressed to facilitate the emergence

†Corresponding author. E-mail: hujun2@nbu.edu.cn

© 2025 Chinese Physical Society and IOP Publishing Ltd. All rights, including for text and data mining, AI training, and similar technologies, are reserved.

of HOTI states. However, FOTI and HOTI states may transform into each other under specific circumstances. For example, in a kagome lattice, the competition between the SOC effect and asymmetric nearest-neighbor hopping can drive a topological phase transition between $\mathbb{Z}_2$ TIs and HOTIs.[35] Similarly, a moderate tensile strain may lead to a topological transition from an HOTI to a QSH insulator in 2D hydrogenated tetragonal stanene.[36] Intuitively, the HOTI states in these systems are not strictly intrinsic properties, as their emergence depends on external conditions such as symmetry breaking, strain, or interlayer coupling. Nevertheless, these observations suggest the potential coexistence of FOTI and HOTI states within $\mathbb{Z}_2$ TIs, hinting at a subtle interplay between these topological orders.

In this work, we investigate the topological properties of freestanding 2D honeycomb Bi and HgTe, as well as $Al_2O_3(0001)$-supported 2D HgTe [HgTe/$Al_2O_3(0001)$]. Our results reveal that all three systems are intrinsic 2D $\mathbb{Z}_2$ TIs, with their 0D nanoflakes exhibiting topological corner states, a robust signature of coexisting first-order and higher-order TI phases. In addition, the spatial distributions of these corner states are strongly influenced by the atomic configurations at the nanoflake edges, which may lead to the emergence of fractional electron charges accumulated at the nanoflake corners. Among the studied systems, HgTe/$Al_2O_3(0001)$ is the most promising candidate, owing to its experimentally feasible geometry and the favorable energy alignment of its corner states, making it a strong contender for applications in next-generation electronic and quantum devices.

2. Methods

The first-principles calculations were carried out in the framework of density-functional theory implemented in the Vienna *ab initio* simulation package (VASP).[37,38] The interaction between valence electrons and ionic cores was described using the projector augmented wave (PAW) method.[39,40] The spin-polarized local density approximate (LDA)[41] was adopted for the exchange–correlation potential and the SOC was invoked self-consistently. The 2D Brillouin zone was sampled by a 36×36 k-grid mesh. The atomic structures were fully relaxed until any component of the forces on a single atom is smaller than 0.01 eV/Å. The Bloch wavefunctions were transformed into maximally localized Wannier functions by using the WANNIER90 code.[42,43] The Wanniertools[44] and PythTB[45] packages were used to construct tight-binding models of materials considered in this work.

3. Results and discussion

Since the 2D honeycomb lattice has been widely explored for hosting HOTI states, we focus on this type of materials. Bismuth monolayer (ML) is a prototypical 2D honeycomb lattice material with strong SOC. To explicitly elucidate the effect of SOC, we first calculated the band structure of 2D honeycomb Bi without including SOC, as shown in Fig. 1(a). It can be seen that the non-relativistic calculation predicts a direct band gap of 421 meV at the Γ point. When the SOC is included, the band structure undergoes significant splitting, as seen in Fig. 1(b), highlighting the strong SOC effect in Bi. Moreover, the band gap transitions from direct to indirect. This is attributed to the substantial Rashba splitting of the topmost valence band near the Γ point, which significantly raises the energy levels around the Γ point, while the energy level at the Γ point remains relatively unchanged. Consequently, the indirect band gap reduces to 237 meV. To investigate the topological nature of 2D honeycomb Bi, we need to calculate the $\mathbb{Z}_2$ topological invariant. Since 2D honeycomb Bi possesses inversion symmetry, the $\mathbb{Z}_2$ topological invariant can be obtained by investigating the parities of the occupied eigenvalues at the time-reversal invariant momenta in the Brillouin zone, as proposed by Fu and Kane.[46] Note that the time-reversal invariant momenta consists of the Γ point and three M points, with the parities of all energy levels at the Γ point and one M point marked in Fig. 1(b). The parities of the energy levels at the other two M points are the same as those in Fig. 1(b). Consequently, we obtained $\mathbb{Z}_2 = 1$, confirming that 2D honeycomb Bi is topologically nontrivial, consistent with previous report.[47–49]

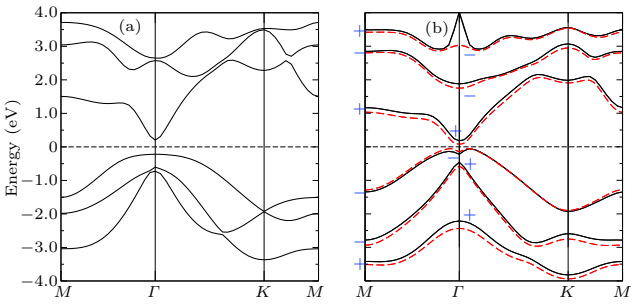


Fig. 1. Band structures of 2D honeycomb Bi (a) without and (b) with spin–orbit coupling. The red dashed curves in panel (b) are the energy bands from tight-binding model with the fitted basis set of relativistic Wannier functions. The "+/−" sign indicates the "even/odd" parity of the energy levels at the time-reversal-invariant momenta (the M and Γ points). The Fermi level (dashed horizontal line) is set as the zero energy.

The bands in Fig. 1 primarily originate from the Bi-6p orbitals, while the bands from the Bi-6s orbitals lie far below Fermi level (E_F). Accordingly, we selected the Bi-6p orbitals as the basis set to construct relativistic Wannier functions (i.e., with the SOC effect included) for tight-binding simulations.[45] Clearly, the tight-binding band structure closely aligns with the DFT bands, as presented in Fig. 1(b). We then calculated the band structures of Bi nanoribbons using the tight-binding method. Similar to graphene, Bi nanoribbons can have either zigzag or armchair edges. Additionally, the widths of the nanoribbons must be sufficiently large to avoid coupling between edge

states. Figure 2 displays the band structures of Bi nanoribbons with zigzag and armchair edges. Notably, several edge bands appear within the bulk TI gap, manifesting the nontrivial topological characteristics, in agreement with previous literature.[47] Furthermore, the edge bands of zigzag and armchair nanoribbons exhibit distinct features due to the different arrangement of edge atoms in the two configurations.

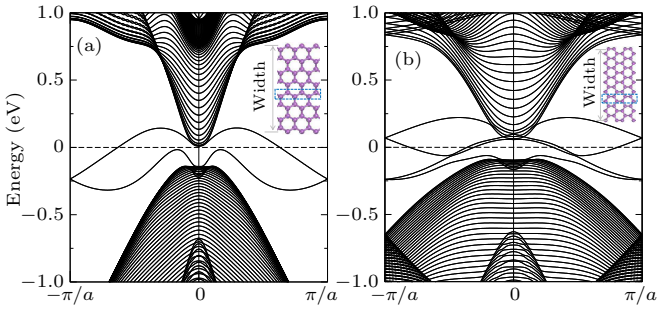


Fig. 2. Band structures of 1D Bi nanoribbons with (a) zigzag and (b) armchair edges. The Fermi level (dashed horizontal line) is set as the zero energy. The insets present the atomic structures of Bi nanoribbons with a width of 8 Bi chains. The blue dashed rectangles in panels (a) and (b) mark one zigzag and armchair Bi chain, respectively. The actual width of the nanoribbons for the band structures is 60 Bi chains.

In general, for a 2D system with inversion and time-reversal symmetries, the higher-order band topology can be characterized by the second Stiefel–Whitney number ω_2, which is also calculated from the parities of the occupied eigenvalues at the time-reversal invariant momenta in the Brillouin zone.[50] Interestingly, we obtained $\omega_2 = 1$ for 2D honeycomb Bi. Therefore, 2D honeycomb Bi is indeed an HOTI and can host topological corner states. To clearly observe the topological corner states, we investigated 0D rhombic nanoflakes, a typical geometry used to reveal HOTI corner states.[19,20] We constructed a series of 0D Bi rhombic nanoflakes with zigzag and armchair edges of varying sizes and found that well-separated corner states emerge when the edge lengths exceed approximately 50 Å. Figure 3 illustrates the energy levels of rhombic nanoflakes with zigzag and armchair edges. In the zigzag nanoflake, the energy levels of the corner states locate at around 0.23 eV above E_F of 2D honeycomb Bi. We further analyzed the spatial distribution of the probability densities of their wavefunctions ($|\varphi_i|^2$). As presented in Fig. 3(a), the wavefunctions of the two corner states are separately localized at the two acute-angle corners of the nanoflake. In contrast, the armchair nanoflake exhibits distinct corner states, as depicted in Fig. 3(b). Here, four nearly degenerate energy levels are observed at approximately 0.304 eV above E_F of 2D honeycomb Bi. The spatial distributions of the probability densities of these wavefunctions are almost identical, with all states localized at both acute-angle corners of the nanoflake. This behavior can be attributed to the high symmetry of the armchair nanoflake, where all edges and corners contain both types of inequivalent Bi atoms. Notably, both the FOTI edge states and HOTI corner states in 2D honeycomb Bi derivatives originate from the intrinsic SOC effect of the material. Therefore, we can conclude that 2D honeycomb Bi inherently host both first- and higher-order topological phases, which coexist without requiring external manipulations.

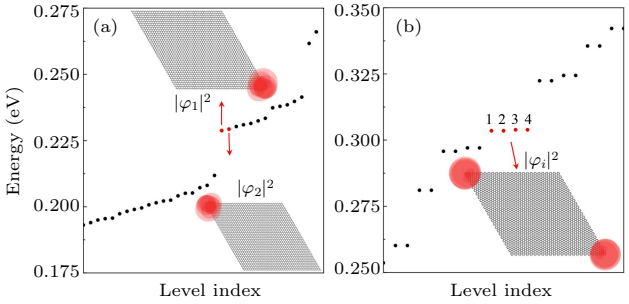


Fig. 3. Energy levels of Bi rhombic nanoflakes with (a) zigzag and (b) armchair edges with respect to the Fermi level. The insets display the spatial distributions of the probability densities of the corner-state wavefunctions ($|\varphi_i|^2$). The widths of the zigzag and armchair nanoflakes are 40 and 25 Bi chains, respectively.

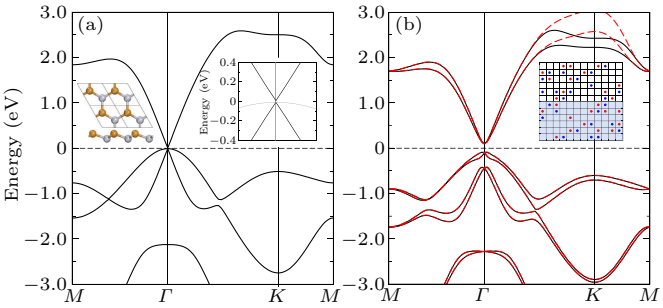


Fig. 4. Band structures of 2D honeycomb HgTe (a) without and (b) with spin–orbit coupling. The red dashed curves in panel (b) are the energy bands from tight-binding model with the fitted basis set of relativistic Wannier functions. The inset in panel (b) zooms in the energy bands near the Γ point. The inset in panel (b) presents the atomic structure of 2D honeycomb HgTe, where the grey and brown spheres stand for Hg and Te atoms, respectively. The inset in panel (b) is the n-field configuration in the Brillouin zone sampled by a 12×12 k-grid mesh. The nonzero points are denoted by red ($n = 1$) and blue ($n = -1$) dots, respectively.

It is important to note that the corner states in Bi nanoflakes are positioned relatively far above E_F, which poses challenges for practical applications. Therefore, it is worthwhile to explore other 2D honeycomb materials that host HOTI states near E_F. Except for elemental materials such as graphene and Bi, several binary compounds, including BN and HgTe, also crystallize into 2D honeycomb lattice.[51] Since 2D honeycomb BN is a wide-band-gap semiconductor, we selected 2D honeycomb HgTe as a representative 2D honeycomb compound to investigate its topological properties. As shown in Fig. 4(a), the band structures of 2D honeycomb HgTe [see its atomic structure in Fig. 4(b)] without SOC exhibits graphene-like Dirac states, with bands dispersing linearly near E_F. Nevertheless, the Dirac states appear at the Γ point rather than the K point in graphene, featuring a small band gap of 17 meV. Analysis of their wavefunctions indicates that these Dirac states originate from hybridization between the s orbitals of Hg and Te, in contrast to graphene, where Dirac states arise from the p_z orbitals of C. The parabolic band just below E_F

primarily derives from the in-plane p_x and p_y orbitals of Hg and Te. Upon including SOC, the bands undergo remarkable splitting due to the strong hybridization between the s and $p_{x/y}$ orbitals mediated by the SOC Hamiltonian. In addition, a band gap of 183 meV is induced by the SOC effect and band inversion occurs at the band gap. To investigate the topological nature of 2D honeycomb HgTe, we employed the so-called "*n*-field" method to compute the $\mathbb{Z}_2$ topological invariant, since inversion symmetry is broken.[52–54] As shown in the inset of Fig. 4(b), the summation over the half Brillouin zone (shadow area) yields $\mathbb{Z}_2 = 1$, demonstrating that 2D honeycomb HgTe is a topologically nontrivial material.

Figure 5 presents the band structures of HgTe nanoribbons with zigzag and armchair edges, calculated using the tight-binding method with the corresponding relativistic Wannier functions. Apparently, both nanoribbons exhibit edge states within the band gap of 2D honeycomb HgTe, but their characteristics differ. In the zigzag nanoribbon, four bands cross the bulk band gap, with two intersecting points at E_F near the Γ point. For the armchair nanoribbon, however, there are only two edge bands with a single intersecting point located precisely at the Γ point. These edge states are obviously distinct from those in Bi nanoribbons, which can be attributed to their different atomic structures. As illustrated in the inset of Fig. 5(a), the two edges of the zigzag nanoribbon are individually terminated by Hg and Te atoms, making them structurally inequivalent. On the contrary, both edges of the armchair nanoribbon are terminated by Hg–Te dimers, as shown in the inset of Fig. 5(b), resulting in equivalent edges.

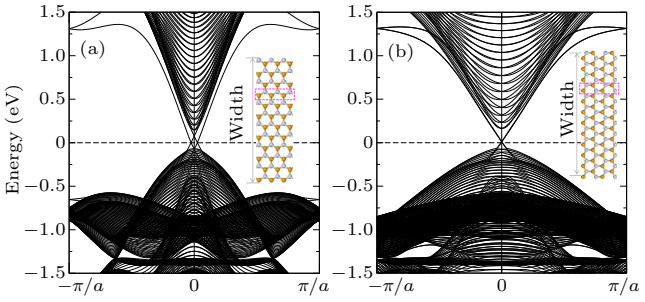


Fig. 5. Band structures of 1D HgTe nanoribbons with (a) zigzag and (b) armchair edges. The insets present the atomic structures of HgTe nanoribbons with a width of 12 Hg–Te chains. The purple dashed rectangles in panels (a) and (b) mark one zigzag and armchair Hg–Te chain, respectively. The actual width of the nanoribbons for the band structures is 60 Hg–Te chains.

Although the second Stiefel–Whitney number ω_2 is widely used to characterize HOTIs in literature, it validates only for systems with inversion and time-reversal symmetries.[50] So far, method to calculate higher-order topological invariant number is not available for systems with inversion symmetry. Therefore, we directly investigated the electronic properties of 0D HgTe rhombic nanoflakes with zigzag and armchair edges to figure out possible corner states. As shown in Fig. 6, all energy levels within the energy range are doubly degenerate due to the reduced structural symmetry compared to Bi nanoflakes. Interestingly, each structure hosts two corner states, demonstrating the coexistence of intrinsic FOTI and HOTI states similar to the case of 2D honeycomb Bi. The energy levels of the corner states are positioned just above E_F, as highlighted by the red dots in Fig. 6. They are the energy levels of the lowest unoccupied molecular orbitals (LUMOs), separated from the highest occupied molecular orbitals (HOMOs) by 41 meV and 114 meV, respectively for the zigzag and armchair nanoflakes. Obviously, these energy levels are much lower than those in Bi nanoflakes, so that they are much easier to be manipulated for applications. The spatial distributions of the two corner states in each structure are identical. In the zigzag nanoflake, both corner states are localized at the acute-angle corner which is terminated by a Te atom, as seen in the set of Fig. 6(a).

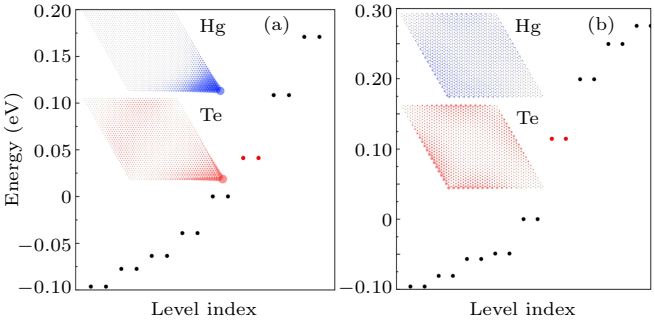


Fig. 6. Energy levels of HgTe rhombic nanoflakes with (a) zigzag and (b) armchair edges, with respect to the Fermi level. The insets display the spatial distributions of the probability densities of the corner-state wavefunctions ($|\varphi_i|^2$) projected on Hg and Te atoms. The widths of the zigzag and armchair nanoflakes are 40 and 25 Hg–Te chains, respectively.

Moreover, it can be seen that the Hg atoms at the corner region contribute most of the corner-state wavefunctions, while only the edge Te atoms near the corner exhibit notable contributions. In contrast, the corner states in the armchair nanoflake primarily originate from the edge Te atoms near the two blunt-angle corners. Accordingly, it is reasonable to presume that these corner states as HOTI states, as generalized from the results for 2D honeycomb Bi. It is worth noting that the spatial distribution of the corner states in the armchair nanoflake appears less localized than those in the zigzag nanoflake. This is likely due to the limited nanoflake size in our calculations, as computational demands increase rapidly with system size. Nevertheless, the primary localization characteristics of the corner states are clearly demonstrated.

Given that freestanding 2D TIs including HgTe are challenging to obtain, it is crucial to identify suitable supporting substrates for potential applications in realistic electronic devices. It has been revealed that $Al_2O_3(0001)$ is an ideal substrate for stabilizing 2D honeycomb HgTe.[51] Since the surface layer of $Al_2O_3(0001)$ consists of both Al and O atoms, there are several sites for both Hg and Te atoms to be adsorbed. We have considered a series of structural configurations and compared their energies to uncover the most stable

atomic structure. We found that HgTe/Al_2O_3(0001) prefers a configuration, with each Hg bonded to three neighboring oxygen atoms and each Te atom bonded to one aluminum atom, and the Hg atoms are close to Al_2O_3(0001) than the Te atoms, as illustrated in Fig. 7(a). The short bond lengths of Hg–O and Te–Al bonds, i.e., $d_1 = 2.70$ Å and $d_2 = 2.74$ Å, indicate strong interaction between HgTe layer and Al_2O_3(0001) substrate. Consequently, the system should no longer be treated as separate entities but rather as an integrated whole. Interestingly, the key feature of the band structure near the Γ point remain intact, as shown in Figs. 7(b) and 7(c), because Al_2O_3(0001) has a wide band gap with its valence band maximum at approximately -0.8 eV below E_F and its conduction band minimum at about 4.2 eV above E_F. In this system, the SOC-induced band gap is 239 meV, and its topological characteristic is preserved with $\mathbb{Z}_2 = 1$ calculated from the "n-field" method. Accordingly, it is appropriate to select the orbitals of HgTe for further investigating the electronic properties of Al_2O_3(0001)-supported HgTe nanoribbons and nanoflakes. The bands obtained from relativistic Wannier function fitting accurately reproduce the corresponding DFT bands, as plotted in Fig. 7(c), confirming that the chosen basis set is indeed sufficient.

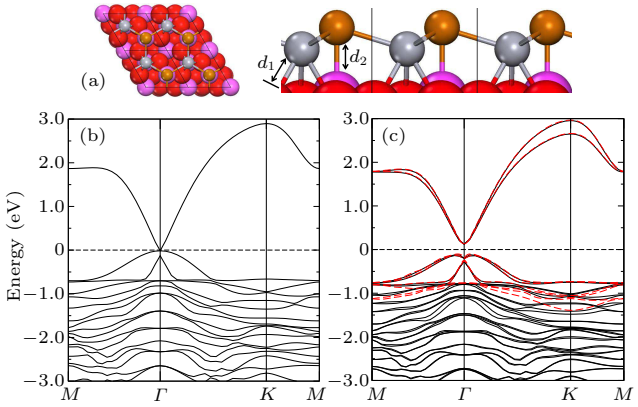


Fig. 7. Structural and electronic properties of 2D honeycomb HgTe on Al_2O_3(0001) substrate. (a) Top and side views of the atomic structure. The grey, brown, purple, and red spheres stand for Hg, Te, Al, and O atoms, respectively. The rhombuses indicate the unit cells. Panels (b) and (c) are band structures without and with spin–orbit coupling, respectively. The red dashed curves in panel (c) are the energy bands from tight-binding model with the fitted basis set of Wannier functions.

The band structures of Al_2O_3(0001)-supported HgTe nanoribbons with zigzag and armchair edges are depicted in Fig. 8. Although they differ from those of freestanding HgTe nanoribbons, the main characteristics of the edge bands are preserved, manifesting that HgTe/Al_2O_3(0001) indeed retains its TI properties. As displayed in Fig. 9, the 0D rhombic nanoflakes also exhibit double-degenerate energy levels, similar to their freestanding counterparts. However, the corner states in both cases are predominantly contributed by Te atoms, while Hg atoms have ignorable contribution. Specifically, the corner states in the zigzag nanoflake arise from Te atoms located near one of the two acute-angle corners, whereas those in armchair nanoflake originate from Te atoms positioned along the edges surrounding the two blunt-angle corners symmetrically. Similar to the free-standing honeycomb HgTe, the spatial distribution of the corner states in the HgTe/Al_2O_3(0001) armchair nanoflake seems extended along the edges, most likely due to the limited nanoflake size in our calculations. In addition, the corner-state energy levels are 19 meV and 47 meV above E_F, respectively for the zigzag and armchair nanoflakes, further reduced compared to those in freestanding HgTe nanoflakes. Such energy levels facilitate low excitation energies for transport in potential device applications.

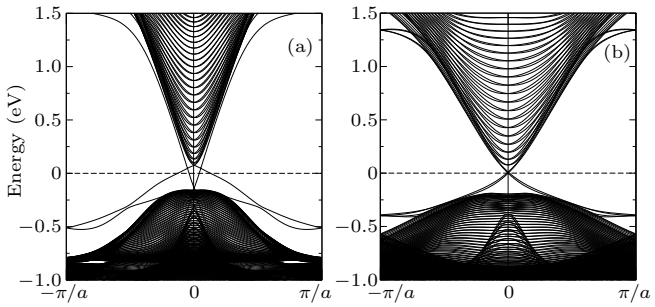


Fig. 8. Band structures of 1D HgTe nanoribbons on Al_2O_3(0001) substrate with (a) zigzag and (b) armchair edges. The widths of the nanoribbons is 60 Hg–Te chains, the same as those in freestanding nanoribbons in Fig. 5.

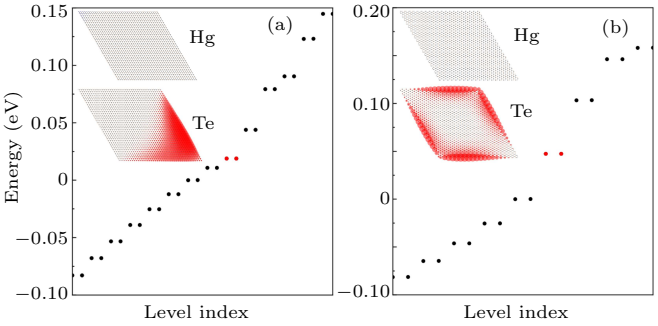


Fig. 9. Energy levels of HgTe rhombic nanoflakes on Al_2O_3(0001) substrate with (a) zigzag and (b) armchair edges, with respect to the Fermi level. The insets display the spatial distributions of the probability densities of the corner-state wavefunctions ($|\varphi_i|^2$) projected on Hg and Te atoms. The widths of the zigzag and armchair nanoflakes are 40 and 25 Hg–Te chains, respectively.

It is known that integrating the probability density of a wavefunction yields the number of electrons associated with that wavefunction, which should be exactly equal to 1 according to quantum mechanics. In the case of armchair nanoflakes of the materials considered in this work, the probability density of an individual corner-state wavefunction is distributed across two opposite corners. However, the two parts are completely separated by the gapped interior region, as shown in Figs. 3(b), 6(b), and 9(c). Consequently, each related corner carries half electron charge, i.e., the fractional electron charge of $\frac{1}{2}e$ might be observed in armchair nanoflakes. In fact, similar fractional electron charges have been reported in graphene nanoflakes, where electron charges of $\frac{1}{2}e$ and $\frac{1}{3}e$ emerge depending on the specific geometries of nanoflakes.[19] It is important to emphasize that, despite the spatial separation, the wavefunction of a single corner state remains an indivisible

quantum entity, with the two fractional electron charges intrinsically entangled. Nevertheless, for certain applications requiring localized charge manipulation, it may be desirable to concentrate the entire electron charge at a single corner. This can be achieved through the application of local perturbations, such as site-specific magnetization or electric potential, to break the symmetry connected by the two corners, as proposed in recent studies.[22] These findings underscore the interplay between geometric confinement, quantum entanglement, and external tunability in the design of functional higher-order topological systems.

4. Conclusions

In summary, we have systematically investigated the topological properties of 2D honeycomb Bi, HgTe, and HgTe/Al_2O_3(0001), based on first-principles calculations and tight-binding simulations. All three systems are intrinsic 2D $\mathbb{Z}_2$ TIs, manifested by the SOC-induced edge states in 1D nanoribbons. Additionally, they exhibit corner states in 0D rhombic nanoflakes, implying the coexistence of first- and higher-order TI states. Notably, the corner states in zigzag nanoflakes are localized at a single corner, whereas those in armchair nanoflakes are distributed across two counter corners. This spatial separation in armchair configurations enables the observation of fractional electron charge of $\frac{1}{2}e$, a phenomenon supported by the bipartite nature of the wavefunctions. However, freestanding 2D honeycomb Bi and HgTe present significant limitations: the corner states in Bi are energetically distant from E_F, and the synthesis of freestanding HgTe remains experimentally challenging. In contrast, the HgTe/Al_2O_3(0001) system offers a promising alternative, as its atomic configuration is experimentally feasible, and its corner states are energetically aligned close to E_F. These attributes make HgTe/Al_2O_3(0001) a promising candidate for next-generation electronic and quantum devices.

Acknowledgements

Project supported by the Program for Science and Technology Innovation Team in Zhejiang Province, China (Grant No. 2021R01004), the Six Talent Peaks Project of Jiangsu Province, China (Grant No. 2019-XCL-081), and the Start-up Funding of Ningbo University and Yongjiang Recruitment Project (Grant No. 432200942).

References

[1] Kane C L and Mele E J 2005 *Phys. Rev. Lett.* **95** 146802
[2] Bernevig B A, Hughes T L and Zhang S C 2006 *Science* **314** 1757
[3] Hasan M Z and Kane C L 2010 *Rev. Mod. Phys.* **82** 3045
[4] Qi X L and Zhang S C 2011 *Rev. Mod. Phys.* **83** 1057
[5] Rachel S 2018 *Rep. Prog. Phys.* **81** 116501
[6] He M, Sun H and He Q L 2019 *Front. Phys.* **14** 43401
[7] Breunig O and Ando Y 2022 *Nat. Rev. Phys.* **4** 184
[8] Benalcazar W A, Bernevig B A and Hughes T L 2017 *Science* **357** 61
[9] Song Z, Fang Z and Fang C 2017 *Phys. Rev. Lett.* **119** 246402
[10] Langbehn J, Peng Y, Trifunovic L, von Oppen F and Brouwer P W 2017 *Phys. Rev. Lett.* **119** 246401
[11] Schindler F, Cook A M, Vergniory M G, Wang Z, Parkin S S P, Bernevig B A and Neupert T 2018 *Sci. Adv.* **4** eaat0346
[12] Ezawa M 2018 *Phys. Rev. Lett.* **120** 026801
[13] Chen R, Chen C Z, Gao J H, Zhou B and Xu D H 2020 *Phys. Rev. Lett.* **124** 036803
[14] Wang K T, Xu F, Wang B, Yu Y and Wei Y 2022 *Front. Phys.* **17** 43501
[15] Dai X and Chen Q 2024 *Phys. Rev. B* **109** 144108
[16] Gao Y, Zhang L, Zhang Y Y and Du S 2024 *Phys. Rev. B* **110** 125103
[17] Wang J D, Li J R, Zhang L L, Jiang C and Gong W J 2024 *Phys. Scr.* **99** 085953
[18] Xie B, Wang H X, Zhang X, Zhan P, Jiang J H, Lu M and Chen Y 2021 *Nat. Rev. Phys.* **3** 520
[19] Liu F and Wakabayashi K 2021 *Phys. Rev. Res.* **3** 023121
[20] Liu B, Zhao G, Liu Z and Wang Z F 2019 *Nano Lett.* **19** 6492
[21] Chen C, Wu W, Yu Z M, Chen Z, Zhao Y X, Sheng X L and Yang S A 2021 *Phys. Rev. B* **104** 085205
[22] Zhou Y and Wu R 2023 *Phys. Rev. B* **107** 035412
[23] Sheng X L, Chen C, Liu H, Chen Z, Yu Z M, Zhao Y X and Yang S A 2019 *Phys. Rev. Lett.* **123** 256402
[24] Lee E, Kim R, Ahn J and Yang B J 2020 *npj Quantum Mater.* **5** 1
[25] Park M J, Jeon S, Lee S, Park H C and Kim Y 2021 *Carbon* **174** 260
[26] Hua C and Xu D H 2025 *Chin. Phys. B* **34** 037301
[27] Chen H, Liu Z R, Chen R and Zhou B 2023 *Chin. Phys. B* **33** 017202
[28] Chen X T, Liu C H, Xu D H and Chen C Z 2023 *Chin. Phys. Lett.* **40** 097403
[29] Schindler F, Wang Z, Vergniory M G, Cook A M, Murani A, Sengupta S, Kasumov A Y, Deblock R, Jeon S, Drozdov I, Bouchiat H, Guéron S, Yazdani A, Bernevig B A and Neupert T 2018 *Nat. Phys.* **14** 918
[30] Yue C, Xu Y, Song Z, Weng H, Lu Y M, Fang C and Dai X 2019 *Nat. Phys.* **15** 577
[31] Canyellas R, Liu C, Arouca R, Eek L, Wang G, Yin Y, Guan D, Li Y, Wang S, Zheng H, Liu C, Jia J and Smith C M 2024 *Nat. Phys.* **20** 1421
[32] Chen C, Song Z, Zhao J Z, Chen Z, Yu Z M, Sheng X L and Yang S A 2020 *Phys. Rev. Lett.* **125** 056402
[33] Han B, Zeng J and Qiao Z 2022 *Chin. Phys. Lett.* **39** 017302
[34] Liu L, An J, Ren Y, Zhang Y T, Qiao Z and Niu Q 2024 *Phys. Rev. B* **110** 115427
[35] Yang Y, Chen X, Pu Z, Wu J, Huang X, Deng W, Lu J and Liu Z 2024 *Phys. Rev. B* **109** 165406
[36] Xu W, Xue Y, Zhu Y, Xu W and Yang Z 2024 *Phys. Rev. Mater.* **8** 074001
[37] Kresse G and Furthmüller J 1996 *Comput. Mater. Sci.* **6** 15
[38] Kresse G and Furthmüller J 1996 *Phys. Rev. B* **54** 11169
[39] Blöchl P E 1994 *Phys. Rev. B* **50** 17953
[40] Kresse G and Joubert D 1999 *Phys. Rev. B* **59** 1758
[41] Perdew J P and Zunger A 1981 *Phys. Rev. B* **23** 5048
[42] Marzari N, Mostofi A A, Yates J R, Souza I and Vanderbilt D 2012 *Rev. Mod. Phys.* **84** 1419
[43] Mostofi A A, Yates J R, Lee Y S, Souza I, Vanderbilt D and Marzari N 2008 *Comput. Phys. Commun.* **178** 685
[44] Wu Q S, Zhang S N, Song H F, Troyer M and Soluyanov A A 2018 *Comput. Phys. Commun.* **244** 405
[45] Coh S and Vanderbilt D Python Tight Binding (PythTB) (2022), Zenodo https://doi.org/10.5281/zenodo.12721315
[46] Fu L and Kane C L 2007 *Phys. Rev. B* **76** 045302
[47] Wada M, Murakami S, Freimuth F and Bihlmayer G 2011 *Phys. Rev. B* **83** 121310
[48] Li X, H, Liu H, Jiang H, Wang F and Feng J 2014 *Phys. Rev. B* **90** 165412
[49] Zhou T, Zhang J, Xue Y, Zhao B, Zhang H, Jiang H and Yang Z 2016 *Phys. Rev. B* **94** 235449
[50] Ahn J, Kim D, Kim Y and Yang B J 2018 *Phys. Rev. Lett.* **121** 106403
[51] Qi C, Ouyang L and Hu J 2018 *2D Mater.* **5** 045012
[52] Fukui T and Hatsugai Y 2007 *J. Phys. Soc. Jpn.* **76** 053702
[53] Xiao D, Yao Y, Feng W, Wen J, Zhu W, Chen X Q, Stocks G M and Zhang Z 2010 *Phys. Rev. Lett.* **105** 096404
[54] Feng W, Wen J, Zhou J, Xiao D and Yao Y 2012 *Comput. Phys. Commun.* **183** 1849